



## **In situ DRIFT studies on N<sub>2</sub>O formation over Cu-functionalized zeolites during ammonia-SCR**

Downloaded from: <https://research.chalmers.se>, 2025-12-04 22:48 UTC

Citation for the original published paper (version of record):








Isapour Toutizad, G., Wang, A., Han, J. et al (2022). In situ DRIFT studies on N<sub>2</sub>O formation over Cu-functionalized zeolites during ammonia-SCR. *Catalysis Science and Technology*, 12(12): 3921-3936. <http://dx.doi.org/10.1039/d2cy00247g>

N.B. When citing this work, cite the original published paper.



Cite this: DOI: 10.1039/d2cy00247g

## *In situ* DRIFT studies on N<sub>2</sub>O formation over Cu-functionalized zeolites during ammonia-SCR†

Ghodsieh Isapour,<sup>a</sup> Aiyong Wang, <sup>b</sup> Joonsoo Han,<sup>b</sup> Yingxin Feng, <sup>c</sup> Henrik Grönbeck, <sup>c</sup> Derek Creaser, <sup>b</sup> Louise Olsson, <sup>b</sup> Magnus Skoglundh <sup>a</sup> and Hanna Härelind <sup>\*a</sup>

The influence of the zeolite framework structure on the formation of N<sub>2</sub>O during ammonia-SCR of NO<sub>x</sub> was studied for three different copper-functionalized zeolite samples, namely Cu-SSZ-13 (CHA), Cu-ZSM-5 (MFI), and Cu-BEA (BEA). The evolution of surface species during the SCR reaction at different temperatures was monitored with step-response experiments using *in situ* diffuse reflectance infrared Fourier transform spectroscopy (DRIFTS) at different reaction conditions. Also, density functional theory (DFT) calculations were performed to assist the interpretation of the experimental results. The DRIFTS results indicate that NO<sup>+</sup> and nitrate species are the main products formed during NO oxidation, and NO appears to adsorb on both Cu-Lewis and Al-Lewis acid sites. The DFT calculations for NO adsorption on the SSZ-13 sample reveal adsorption at Brønsted acid sites with similar adsorption energies but with a slight difference in NO<sup>+</sup> stretching vibrations in the DRIFT spectra. Within the standard SCR reaction, in the O–H stretching region, the number of NH<sub>3</sub> molecules adsorbed on the Brønsted acid sites is higher for the small-pore size sample compared to the medium- and large-pore zeolites. The obtained DRIFTS results for nitrate species are supported by DFT calculations by simulating the IR spectra of mobile and framework bound nitrate species, which both have a signature at 1604 cm<sup>−1</sup> associated with the O–N bond on NO<sub>3</sub><sup>−</sup>. It is revealed that N<sub>2</sub>O is produced in a higher amount at lower temperatures for all three samples irrespective of the NO/NO<sub>2</sub> ratio. Furthermore, the obtained results from both DRIFTS studies and flow reactor experiments show the higher formation of N<sub>2</sub>O for the large-pore zeolite compared to the medium- and small-pore zeolite.

Received 4th February 2022,  
Accepted 3rd May 2022

DOI: 10.1039/d2cy00247g

rsc.li/catalysis

## 1. Introduction

Selective catalytic reduction using ammonia as a reducing agent (NH<sub>3</sub>-SCR) is a widely used technique to abate NO<sub>x</sub> (NO and NO<sub>2</sub>) emissions from both stationary and mobile sources, such as diesel engines.<sup>1,2</sup> In the SCR reaction, however, unwanted byproducts like nitrous oxide (N<sub>2</sub>O), can be formed. This is a problem particularly as N<sub>2</sub>O is a strong greenhouse gas and causes depletion of the ozone layer.<sup>3–5</sup> Although the annual emissions of N<sub>2</sub>O are much lower than those of CO<sub>2</sub>, the global warming potential (GWP) of N<sub>2</sub>O is 310 times

higher than that of CO<sub>2</sub>.<sup>3,5</sup> The concentration of N<sub>2</sub>O in the atmosphere has consistently increased due to natural and anthropogenic activities by 0.2% per year.<sup>3</sup> Owing to the mentioned reasons, it is important to minimize N<sub>2</sub>O formation as a by-product in the SCR reaction.

Nowadays, this can be done by using zeolites with various pore-size that are ion-exchanged with transition metal cations like Cu and Fe. The zeolite framework structure plays a decisive role in determining the properties of copper-functionalized zeolite catalysts for NH<sub>3</sub>-SCR. In general, small-pore (8-membered ring windows) zeolite catalysts (such as Cu-SSZ-13), represent higher durability during hydrothermal aging conditions, premier N<sub>2</sub> selectivity with less N<sub>2</sub>O formation, and excellent hydrocarbon tolerance, compared to medium (10-membered ring windows) or large-pore (12-membered ring windows) zeolites such as Cu-ZSM-5 and Cu-BEA, respectively.<sup>1,6,7</sup> Both the exchanged transition metal cations and the Brønsted acid sites are important for the SCR reactions.<sup>1,8</sup> Zhang and Yang have analyzed the N<sub>2</sub>O formation pathways in NH<sub>3</sub>-SCR over different catalysts (Cu-ZSM-5, Fe-ZSM-5, Cu-SAPO-34, Fe-SAPO-34, Cu-SSZ-13, and Fe-

<sup>a</sup> Department of Chemistry and Chemical Engineering, Division of Applied Chemistry Competence Centre for Catalysis, Chalmers University of Technology, Gothenburg, Sweden. E-mail: hanna.harelind@chalmers.se

<sup>b</sup> Department of Chemistry and Chemical Engineering, Division of Chemical Engineering, Competence Centre for Catalysis, Chalmers University of Technology, Gothenburg, Sweden

<sup>c</sup> Department of Physics, Division of Chemical Physics, Competence Centre for Catalysis, Chalmers University of Technology, Gothenburg, Sweden

† Electronic supplementary information (ESI) available. See DOI: <https://doi.org/10.1039/d2cy00247g>



SSZ-13), and the results indicated that for most of the Cu catalysts, the main  $\text{N}_2\text{O}$  formation pathway at higher temperatures is the non-selective catalytic oxidation of  $\text{NH}_3$ .<sup>2</sup> Non-selective behavior takes place when other products (specifically  $\text{N}_2\text{O}$ ) are formed rather than  $\text{N}_2$ , *e.g.* during standard or fast SCR reaction conditions or when the converted  $\text{NO}/\text{NH}_3$  molar ratio is lower than 1.<sup>2</sup>

In the temperature range 250–350 °C, the  $\text{N}_2\text{O}$  formation partially stems from the decomposition of ammonium nitrate (AN).<sup>9</sup> Furthermore,  $\text{NH}_3$ -SCR over Cu-BEA, Cu-SAPO-34, and Cu-SSZ-13 has been investigated by Leistner *et al.*<sup>6</sup> Various reactions like NO oxidation, ammonia oxidation, standard SCR, fast SCR, and  $\text{NO}_2$ -SCR were studied to investigate the influence of the zeolite type on the  $\text{N}_2\text{O}$  formation. The obtained results proposed that  $\text{N}_2\text{O}$  formation takes place on different copper sites or proceeds *via* different mechanisms depending on the temperature. They observed that increasing the temperature above 300 °C resulted in a higher  $\text{N}_2\text{O}$  formation for Cu-SAPO-34 followed by Cu/SSZ-13 and Cu-BEA samples. The results indicate a higher formation of ammonium nitrate at low temperatures and its subsequent decomposition at higher temperatures. To sum up, the choice of type of zeolite/zeotype and reaction temperature affects the activity and selectivity of the different steps in the SCR process.

Density functional theory (DFT) calculations have also been used to identify the fundamental reaction pathways of the SCR reaction.<sup>10,11</sup> Recently, Feng *et al.*<sup>8</sup> proposed a reaction mechanism at low temperatures for  $\text{N}_2\text{O}$  formation over the small-pore zeolite Cu-CHA based on DFT calculations and related the  $\text{N}_2\text{O}$  formation to  $\text{H}_2\text{NNO}$  decomposition over  $(\text{NH}_3)_2\text{Cu}-\text{OOH}-\text{Cu}(\text{NH}_3)_2$  complexes. This can explain why the formation of  $\text{N}_2\text{O}$  increases with increasing copper loading at low temperatures.

The present work aims at investigating the influence of the zeolite framework on the formation of  $\text{N}_2\text{O}$  during ammonia SCR of  $\text{NO}_x$ . For this purpose, three different zeolite samples with varying framework structures: Cu-SSZ-13 (CHA), Cu-ZSM-5 (MFI), and Cu-BEA (BEA) are exposed to  $\text{NH}_3$ -SCR reaction conditions in step-response experiments where the evolution of surface species simultaneously is followed by *in situ* diffuse reflectance infrared Fourier transform spectroscopy (DRIFTS). The samples are exposed to gas sequences corresponding to standard and fast SCR reaction conditions in the temperature range of 130–200 °C. In addition, flow reactor studies are performed to evaluate the  $\text{N}_2\text{O}$  formation during  $\text{NH}_3$ -SCR reaction conditions. Furthermore, the binding energy of different surface species during  $\text{NH}_3$  adsorption are together with vibrational properties obtained by density functional theory calculations.

## 2. Experimental

### 2.1. Sample preparation

Three different copper-functionalized zeolite samples, Cu-SSZ-13, Cu-ZSM-5, and Cu-BEA were prepared according to

the following procedure. The synthesis of Na-SSZ-13 with a Si/Al molar ratio of 12 was performed *via* sol-gel and hydrothermal crystallization in an autoclave. First, 1 M NaOH was prepared by mixing NaOH (Sigma-Aldrich, >98% anhydrous) in Milli-Q water (18 M $\Omega$  cm). Then, the structure-directing agent (SDA) (25% solution of SDA 2825, Sachem, ZeoGen), aluminum hydroxide (Sigma-Aldrich, 50.0–57.5% Al (as  $\text{Al}_2\text{O}_3$ ) basis, reagent grade), and fumed silica (Sigma-Aldrich, S5130-500G, 0.007  $\mu\text{m}$ , standard grade) were subsequently added to the solution, which was stirred vigorously until a homogenized gel was formed. The obtained gel was transferred to a 125 ml Teflon-lined stainless-steel autoclave, sealed off, and heated to 160 °C for 96 h under stirring to accomplish hydrothermal synthesis. The autoclave was subsequently cooled to room temperature. In this synthesis method, continuous stirring is crucial to achieving a uniform Na-SSZ-13 sample. The obtained slurry was washed three times with Milli-Q water, and the solid/liquid mixture was separated by centrifugation. The resulting precipitate was dried at 110 °C overnight and calcined at 600 °C to remove all SDA. The prepared powder was then dissolved in Milli-Q water and ammonium nitrate (Sigma-Aldrich, 98%, hemi(pentahydrate)), and nitric acid (Sigma-Aldrich, 69%), were added to adjust the pH. The solution was stirred for 1 h (700 rpm) at 80 °C and thereafter washed with Milli-Q water and centrifuged. This step was repeated two times to remove all sodium from the sample. The remaining precipitate was kept at 110 °C overnight to obtain  $\text{NH}_4$ -SSZ-13.

For the preparation of the Cu-SSZ-13 sample, incipient wetness impregnation was used to functionalize the zeolite with copper. First, a copper nitrate solution (Sigma-Aldrich, 98%) was added to the specific amount of  $\text{NH}_4$ -SSZ-13 and then, 3 g of ethanol was added to the mixture. The slurry was stirred for 15 min and then kept at room temperature overnight and thereafter calcined. The calcination of the Cu-SSZ-13 sample was carried out in two steps. The temperature was first increased from room temperature to 600 °C with a rate of 2 °C  $\text{min}^{-1}$  and kept constant for 6 h, and then increased to 750 °C and kept constant for 2 h after which the sample was cooled to room temperature. The other two zeolites ( $\text{NH}_4$ -ZSM-5; Si/Al = 11.5,  $\text{NH}_4$ -BEA; Si/Al = 12.5) were commercially available (Zeolyst international, CBV; 2314 and CP; 814E, respectively), and the functionalization with copper was performed using the same method as used for Cu-SSZ-13. The only difference was the calcination temperature for these two zeolites, which was carried out in one step at 600 °C for 8 h. All samples were degreened under 400 ppm NO, 400 ppm  $\text{NH}_3$  and 10%  $\text{O}_2$  at 200 °C, before being used in the DRIFTS studies.

For the flow reactor experiments, the prepared powder samples were coated on honeycomb-structured cordierite monolith substrates (400 cpsi). Before wash-coating, the monolith substrates were cut to a dimension of 20 mm in length and 15 mm in diameter, and subsequently heated in air at 600 °C for 2 h to eliminate any contaminations. After cooling to room temperature, the monolith substrates were



coated with a slurry including a solid phase composed of the powder sample and boehmite binder (Dispersal P2) with a mass ratio of 95:5 and a liquid phase containing equal amounts of Milli-Q water and ethanol. The monolith was coated by dipping into the slurry to fill all the channels thoroughly. Thereupon, to remove the excess slurry and hinder channel blockage, the coated monolith was dried at 80 °C for 2 min with a heating gun. The process of wash-coating and drying was continued until reaching the aimed loading of wash-coat (~300 mg). Moreover, the coated monoliths were weighed after heating at 500 °C for 1 min and finally calcined in air at 500 °C for 2 h, starting at room temperature with a heating rate of 2 °C min<sup>-1</sup>.

## 2.2. Sample characterization

Powder X-ray diffraction (XRD) measurements were performed using a Siemens diffractometer D5000 operating at 40 kV and 40 mA with Cu K $\alpha$  radiation ( $\lambda = 1.5418$  Å). Data were collected with  $2\theta$  ranging from 5 to 50° using a step size of 0.02. Scanning electron microscopy (SEM) images were obtained using an LEO Ultra 55 SEM equipped with an energy dispersive X-ray (EDX) system (Oxford Inca). A Tristar 3000 (Micromeritics) instrument was used to obtain N<sub>2</sub> adsorption and desorption isotherms at 77 K. All fresh powder samples were degassed at 250 °C for 10 h under the flow of N<sub>2</sub>. The Brunauer–Emmett–Teller (BET) and Barrett–Joyner–Halenda (BJH) methods were applied to determine the specific surface area and the pore volume, respectively, which were obtained from the  $t$ -plot method and by measuring the multilayer adsorption of N<sub>2</sub>. Although the BET method is beneficial for determining specific surface areas, it can be confusing due to the difficulty of forming multilayers on the internal surface of microporous materials such as small-pore zeolites. Elemental analysis of the samples was performed using inductively coupled plasma sector field mass spectrometry (ICP-SFMS) by ALS Scandinavia AB in Luleå, Sweden.

*In situ* DRIFTS was used to follow the evolution of surface species on the samples during reaction conditions. The DRIFTS measurements were performed with a VERTEX70 spectrometer (Bruker), equipped with liquid nitrogen cooled mercury cadmium telluride (MCT) detector with the bandwidth of 600–12 000 cm<sup>-1</sup>, and a high-temperature stainless steel reaction chamber (Harrick Scientific Products Inc.) with CaF<sub>2</sub> windows. The measurement of all spectra was done between 400 and 4000 cm<sup>-1</sup> with a spectral resolution of 1 cm<sup>-1</sup> and the reported spectra are obtained by an average of 90 scans. The approximate amount of sample loaded into the reaction chamber was 100 mg. The samples were pretreated in 10 vol% O<sub>2</sub>, with Ar as a carrier gas, for 1 h at 500 °C to remove impurities from the surface of the sample, and subsequently cooled to reaction temperature in Ar. Background spectra were taken under Ar at 200, 180, 150, and 130 °C. Gases were introduced to the reaction chamber by individual mass flow controllers (HiTech), and the total

flow was 100 ml min<sup>-1</sup> (balanced with Ar). The evolution of surface species on the samples was measured at the mentioned temperatures during step-response experiments with 15 min length for each step, as shown in Table 1. In the first step, the sample was exposed to NO at 200 °C for 15 min using a feed consisting of 10 vol% O<sub>2</sub>, 400 ppm NO, and Ar as balance. During the NO exposure, IR spectra were collected by varying exposure time using the related background spectra taken before the introduction of NO. In the second step, the sample was exposed to a full standard NH<sub>3</sub>-SCR feed by introducing 400 ppm NH<sub>3</sub> in the presence of 400 ppm NO, 10 vol% O<sub>2</sub> and Ar for 15 min. The experiment continued by switching off the NO feed for 15 min in the third step and then switching on the NO feed again to have a second full standard NH<sub>3</sub>-SCR feed for 15 min in the fourth step. Directly following, the sample was exposed to 200 ppm NO, 200 ppm NO<sub>2</sub> and 10 vol% O<sub>2</sub> for 15 min in the fifth step before the addition of NH<sub>3</sub> in the sixth step for having a full fast NH<sub>3</sub>-SCR feed for 15 min. This step was followed by the final seventh step where the sample was exposed to 400 ppm NH<sub>3</sub> in Ar for 15 min. The outlet gas composition was continuously analyzed by mass spectrometry (MS) using a Hidden Analytical, HPS-20 QIC instrument following the  $m/z$  ratios 17 (NH<sub>3</sub>), 28 (N<sub>2</sub> and CO), 30 (NO), 32 (O<sub>2</sub>), 40 (Ar), 44 (N<sub>2</sub>O and CO<sub>2</sub>) and 46 (NO<sub>2</sub>). The experimental procedure is summarized in Table 1.

The quantification of DRIFTS data for the formation of N<sub>2</sub>O, NO<sup>+</sup> and nitrate species was done by integrating the attributed peak area in the wavenumber range of 2237 cm<sup>-1</sup> with a shoulder at 2208 cm<sup>-1</sup>, 2050–2150 cm<sup>-1</sup>, and 1530–1700 cm<sup>-1</sup>, respectively, at the steady-state of the reaction.

## 2.3. Flow reactor experiments

After wash-coating, the monolith samples were degreased in standard SCR conditions for 2 h at 500 °C, starting at room temperature with a heating rate of 20 °C min<sup>-1</sup>. The catalytic activity was measured in a flow reactor consisting of a horizontal quartz tube placed in a heating coil and covered with an isolating material, which was equipped with several Bronkhorst mass flow controllers and a controlled evaporation and mixing (CEM) system for controlling the supply of gases and dosing water vapor, respectively. An FTIR spectrometer (MKS Multigas 2030 HS) was used to analyze the reactor outlet gas concentrations. A LabVIEW interface was used for controlling the setup system. The temperature of the sample and the inlet gas flow were measured by a type-K thermocouple placed in the central channel of the monolith sample and 15 mm upstream of the catalyst in the gas phase, respectively. For all experiments, a total flow of 1200 ml min<sup>-1</sup> (gas hourly space velocity of 20 400 h<sup>-1</sup>) was used with Ar as a balance to attain constant total flow. The pretreatment of the samples was performed in the presence of 10 vol% O<sub>2</sub> in Ar for 20 min at 500 °C before the standard and fast SCR reaction.



**Table 1** Inlet gas composition for step-response experiments in the DRIFTS cell

	Feed composition	Exposure time
1. NO oxidation	400 ppm NO, 10 vol% O <sub>2</sub>	15 min
2. Standard SCR	400 ppm NO, 400 ppm NH <sub>3</sub> , 10 vol% O <sub>2</sub>	15 min
3. NH <sub>3</sub> adsorption	400 ppm NH <sub>3</sub> , 10 vol% O <sub>2</sub>	15 min
4. Standard SCR	400 ppm NO, 400 ppm NH <sub>3</sub> , 10 vol% O <sub>2</sub>	15 min
5. NO <sub>2</sub> adsorption	200 ppm NO, 200 ppm NO <sub>2</sub> , 10 vol% O <sub>2</sub>	15 min
6. Fast SCR	200 ppm NO, 200 ppm NO <sub>2</sub> , 400 ppm NH <sub>3</sub> , 10 vol% O <sub>2</sub>	15 min
7. NH <sub>3</sub> adsorption	400 ppm NH <sub>3</sub> , 10 vol% O <sub>2</sub>	15 min

The standard NH<sub>3</sub>-SCR experiments were carried out isothermally at 130, 150, 180, and 200 °C by exposing the sample to 400 ppm NH<sub>3</sub>, 400 ppm NO, 10 vol% O<sub>2</sub> in Ar for 1 h. Then, the reactor temperature was increased stepwise to 200 °C with a 20 °C increment and kept constant at each step for 30 min, to measure the NO<sub>x</sub> conversion and N<sub>2</sub>O formation. Further on, fast SCR experiments were performed by exposing the sample to 400 ppm NH<sub>3</sub>, 200 ppm NO, 200 ppm NO<sub>2</sub>, 10 vol% O<sub>2</sub> in Ar for 1 h. The experimental procedure was the same as for standard SCR.

#### 2.4. DFT calculations

Spin-polarized density functional theory calculations were carried out using the Vienna *ab initio* simulation package (VASP).<sup>12–15</sup> The projector augmented wave (PAW)<sup>16,17</sup> method was used to describe the interaction between the valence electrons and the core and the valence electrons were expanded with a plane wave basis set up to a cutoff energy of 480 eV. The number of valence electrons treated in the calculations was Cu(11), Si(4), Al(3), O(6), N(5), and H(1). Only the gamma point was used in the *k*-point sampling.

Exchange–correlation effects were described using the gradient-corrected Perdew–Burke–Ernzerhof (PBE) functional,<sup>18</sup> augmented Grimme-D3 corrections to describe van der Waals interactions,<sup>19,20</sup> and a Hubbard-U term for Cu 3d. Based on previous work, the *U*-parameter was set to 6 eV.<sup>21</sup> The convergence criterion in the self-consistent-field cycles was set to  $1 \times 10^{-5}$  eV and the structures were relaxed until the force on each atom was lower than 0.02 eV Å<sup>-1</sup>. Frequency analyses were performed on the optimized models. The Zenodo program was used to obtain the vibrational intensities.<sup>22</sup> A rhombohedral unit cell, including

12 tetrahedral Si-sites was used to describe the chabazite structure. The lattice parameters were fixed experimentally determined values ( $\alpha = \beta = \gamma = 94.2^\circ$ ,  $a = b = c = 9.42 \text{ \AA}$ ). To model Cu-exchanged SSZ-13 or H-SSZ-13, one or two Si atoms in the six-membered ring of the zeolite cage were substituted by Al giving a Si/Al ratio of 11 or 5. The chosen Si/Al ratios are within the experimental range<sup>23–25</sup> and therefore, a reasonable model for the Cu-SSZ-13 material.

### 3. Results and discussion

#### 3.1. Catalyst characterization

Table 2 displays for the powder samples, the Cu loading, Si/Al ratio, and Cu/Al ratio, obtained from the ICP-SFMS analysis, and the specific surface area and specific pore volume, obtained from the nitrogen sorption analysis. The Cu content, Si/Al ratio and Cu/Al ratio are  $2.07 \pm 0.08 \text{ wt\%}$ ,  $10.8 \pm 0.9$  and  $0.30 \pm 0.04$ , respectively, which is close to the target values. The specific pore volume is significantly higher for the H-SSZ-13 and Cu-SSZ-13 samples compared to the samples based on ZSM-5 or BEA, which is owing to the characteristic large cage void in the CHA-type framework.<sup>26</sup> A decrease in specific surface area is observed upon Cu loading as compared to the zeolites in the H-form (almost 20% of surface area loss). This is due to the presence of Cu species, such as Cu<sup>2+</sup> and [Cu (OH)]<sup>+</sup> in the cages of the zeolite framework and consequently less amount of N<sub>2</sub> can adsorb.<sup>27</sup> However, the obtained results do not represent a diverse transformation of the microporous structure upon copper ion exchange.<sup>26,27</sup>

Fig. S1 (see ESI†) shows SEM images of the Cu-SSZ-13, Cu-ZSM-5, and Cu-BEA powder samples. The O, Al, Si, and Cu content of the crystals obtained from the SEM-EDX analysis is summarized in Table S1†. Based on EDX results, although the Si/Al ratio is close to the ICP-SFMS results (11.8, 12.2, 11.8, for Cu-SSZ-13, Cu-ZSM-5, and Cu-BEA, respectively), the Cu/Al ratio (0.198, 0.27, 0.29, for Cu-SSZ-13, Cu-ZSM-5, and Cu-BEA, respectively) is lower compared to the ICP-SFMS analysis, which can be due to the fact that only a small area is analyzed in the EDX measurements. The results obtained from the XRD analysis of the powder samples (Fig. S2†) provide the diffraction patterns for the parent zeolite samples which are characteristic for H-SSZ-13, H-ZSM-5, and H-BEA (JCPDS no.; 52-0784,<sup>28</sup> 89-1421<sup>29</sup> and 48-0038,<sup>30</sup> respectively) samples. Furthermore, the diffractograms show that the

**Table 2** Copper content, Si/Al ratio, Cu/Al ratio, specific surface area and specific pore volume of the samples

Sample	Cu content (wt%)	Si/Al ratio	Cu/Al ratio	Specific surface area (m <sup>2</sup> g <sup>-1</sup> )	Specific pore volume (cm <sup>3</sup> g <sup>-1</sup> )
Cu-SSZ-13	1.99	11.4	0.28	540	0.23
Cu-ZSM-5	2.13	10.6	0.28	323	0.12
Cu-BEA	2.10	9.94	0.34	508	0.15
H-SSZ-13	—	10.0	—	674	0.30
H-ZSM-5	—	11.3	—	425	0.16
H-BEA	—	11.5	—	631	0.19





structure of the samples is maintained after functionalization with copper and there is no distinct intensity increase or broadening of the diffraction peaks upon adding Cu to the parent zeolites (H-type). There are no diffraction peaks of crystalline CuO (CuO: highest peaks at *ca.* 2 $\theta$  = 35.6 and 38.8),<sup>31,32</sup> which indicates that copper is well dispersed in the Cu-functionalized samples or it is in amorphous form. The other possibility is that the amount of CuO is too low to be detected by the diffractometer.

### 3.2. Evolution of surface species during NH<sub>3</sub>-SCR step response experiments

The interaction of feed gas species (*i.e.*, NO, NO<sub>2</sub> and NH<sub>3</sub>) with the surface of the copper-functionalized samples was followed by *in situ* DRIFTS during NH<sub>3</sub>-SCR step response experiments. Fig. 1 shows the IR spectra in the 2300–1300 cm<sup>−1</sup> region after exposing the Cu-SSZ-13, Cu-ZSM-5, and Cu-BEA samples to 400 ppm NO and 10% O<sub>2</sub> for 15 min at 200, 180, 150, and 130 °C. The spectra in the entire wavenumber region for the experiment performed at 200 °C are shown in Fig. S4.† Starting with the spectrum for the Cu-SSZ-13 sample obtained at 200 °C, an absorption band around 2156 cm<sup>−1</sup> can be observed. This band becomes more intense when the exposure temperature is decreased and evolves to two absorption peaks, positioned at 2156 with a shoulder at 2185 cm<sup>−1</sup>, at 130 °C. Based on the literature, the peak at 2156 cm<sup>−1</sup> has been attributed to N–O stretching vibrations of NO adsorbed on Cu-Lewis acid sites (Cu<sup>2+</sup>) over Cu-based zeolites.<sup>9,33</sup>

An alternative interpretation suggests the possibility of two cationic positions existing in the zeolite.<sup>9</sup> Kwak *et al.*<sup>34</sup> observed the presence of cationic sites of Cu<sup>2+</sup> ions in Cu-SSZ-13 with different reducibility, which can have interaction with NO. The interaction can happen either inside the six-membered rings or in the super cages in front of the six-membered ring.

For the Cu-ZSM-5 sample, the corresponding spectra show a less intense band centered at 2145 cm<sup>−1</sup>, which also becomes more intense when the exposure temperature is decreased. The Cu-BEA sample shows a weak band at 2154 cm<sup>−1</sup>, which becomes only slightly more intense with decreasing temperature. By moving from a small pore-zeolite to a large-pore zeolite, it is clearly seen that the intensity of the peak attributed to NO adsorbed on Cu<sup>2+</sup> decreases.

Comparing the parent zeolites reveals peaks at 2196 and 2089 cm<sup>−1</sup> for H-SSZ-13, attributed to N–O stretching vibrations of NO adsorbed on Al–O–Al sites (Al-Lewis acid sites). DRIFTS spectra during NO oxidation at 200 °C for H-type zeolites are shown in Fig. S5.† The results for N–O stretching vibrations of NO<sup>+</sup> for the H-ZSM-5 and H-BEA samples show a single peak at 2162 and 2195 cm<sup>−1</sup>, respectively, which also can be related to NO adsorbed on Brønsted acid sites. All samples show two absorption peaks around 1620 and 1570 cm<sup>−1</sup>. Both peaks become more intense with decreasing exposure temperature. These peaks are commonly attributed to N–O stretching vibrations of surface nitrate species.<sup>35,36</sup> The band around 1620 cm<sup>−1</sup> could be characterized as symmetric O–N–O–N–O vibrations, and the one around 1570 cm<sup>−1</sup> is attributed to N–O vibrations from adsorbed asymmetric N<sub>2</sub>O<sub>3</sub> species.<sup>37</sup>

The exact identification of peaks in the nitrate region is not straightforward as the different nitrate species (*i.e.*, monodentate nitrates, bridging monodentate, chelating, and bridging bidentate nitrates) have overlapping vibrations. Wang *et al.*<sup>35</sup> investigated the interaction between NO and Cu-SAPO-34 and observed three peaks in the 1650–1500 cm<sup>−1</sup> wavenumber region after the exposure to NO and O<sub>2</sub>. These peaks were assigned to surface nitrate and nitro species. Furthermore, Chen *et al.*<sup>7</sup> compared the catalytic reaction for NO oxidation over Cu-CHA and Cu-BEA during NH<sub>3</sub>-SCR reaction conditions and recognized one group of peaks in the

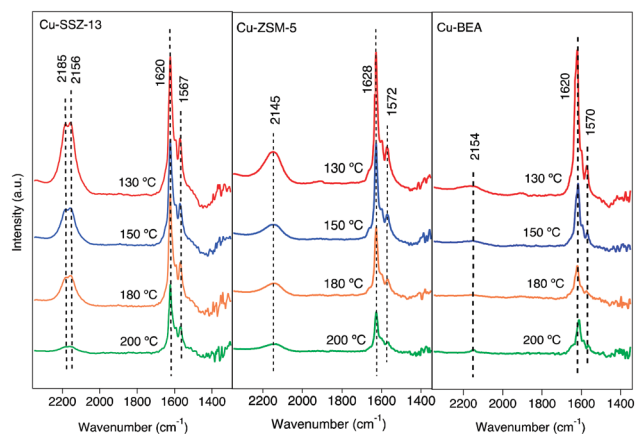


Fig. 1 *In situ* DRIFT spectra after exposing the Cu-SSZ-13, Cu-ZSM-5, and Cu-BEA samples to 400 ppm NO and 10% O<sub>2</sub> for 15 min at 200, 180, 150, and 130 °C.

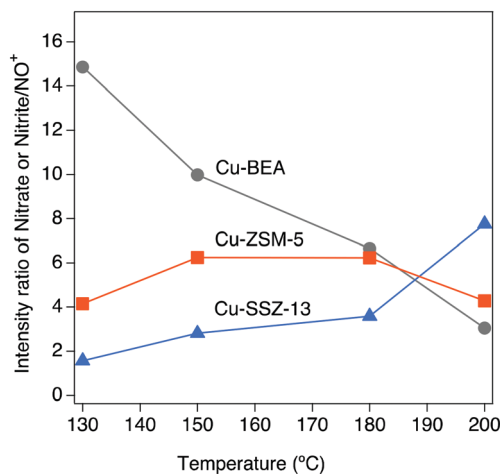


Fig. 2 The effect of temperature on the intensity ratio of nitrate or nitrite/NO<sup>+</sup> during exposure of the Cu-SSZ-13, Cu-ZSM-5, and Cu-BEA samples to 400 ppm NO and 10% O<sub>2</sub> for 15 min at 200, 180, 150, and 130 °C.



1550–1600  $\text{cm}^{-1}$  region that was attributed to different configurations of surface nitrates.

As can be seen from Fig. 1, the intensities of the bands decrease with increasing temperature. Since comparing the behavior of different samples based on the intensity of the absorption peaks is difficult, the intensity ratio of these two distinct bands (nitrate, nitrite/ $\text{NO}^+$ ) has been analyzed and an interesting trend emerged, which is depicted in Fig. 2. It is clear that all three samples represent various behavior at low and high temperatures. At 130 °C, the peak ratio is higher for the Cu-BEA compared to the Cu-ZSM-5 and Cu-SSZ-13 samples, which decreases by increasing temperature. The Cu-ZSM-5 sample shows an increase from 130 °C to around 165 °C and then proceeds through a maximum and eventually (at 200 °C) reaches a similar ratio as for 130 °C. However, for the Cu-SSZ-13 sample, an increasing trend starts from 130 °C and reaches its maximum at 200 °C. Changes in the peak ratio attributed to nitrate or nitrite/ $\text{NO}^+$  species by increasing temperature can likely be owing to a change in the relative abundance of  $\text{NO}^+$  with increasing temperature. The large-pore zeolite sample (Cu-BEA) shows a decrease in this ratio, as compared to the small-, and medium-pore zeolites (Cu-CHA and Cu-MFI). This indicates that at low temperature,  $\text{NO}^+$  is stabilized to a higher degree in the small-pore zeolite than in the medium- and large-pore zeolites, and by increasing temperature the relative  $\text{NO}^+$  value decreases for small-pore zeolite and increases for large-pore zeolite. This can probably be owing to the higher stability of  $\text{NO}^+$  at low temperature for SSZ-13 catalyst and its higher stability for the large-pore zeolite at the higher temperature, whereas Cu-ZSM-5 shows maximum  $\text{NO}^+$  coverage at intermediate temperature. The values for the peak intensity of two distinct peaks in Fig. 1 ( $\text{NO}^+$  ~2150 and nitrate species ~1624) have been evaluated individually and are shown in supplementary information at Fig. S3(a) and (b).†

In addition, in Fig. S4,† a weak negative band is observed for Cu-SSZ-13 at 3653  $\text{cm}^{-1}$ , which likely is caused by the depletion of Brønsted acid sites (Si–OH–Al) due to the interaction of  $\text{NO}^+$  with protons.<sup>23,35,38</sup>

The addition of 400 ppm  $\text{NH}_3$  to the 400 ppm  $\text{NO} + 10\%$   $\text{O}_2$  feed (experiment 2, Table 1) resulted in the development of a series of absorption peaks for all three samples, which is shown in Fig. S6† for the O–H stretching (a), N–H stretching (b) and N–H bending (c) wavenumber regions. The evolution of peaks *versus* time is shown in Fig. S7.† Adsorbed ammonia provides information on surface acid sites and their corresponding acidity.<sup>39</sup> For all samples, IR features appear at two different regions related to ammonia species after the sample was exposed to 400 ppm  $\text{NH}_3$ , 400 ppm  $\text{NO}$ , 10%  $\text{O}_2$  in Ar for 15 min. For adsorbed ammonia, the bands at high wavenumbers (higher than 3000  $\text{cm}^{-1}$ ) are related to N–H stretching vibrations, and the bands at lower wavenumbers are attributed to N–H bending vibrations. The negative peaks at 3579 and 3608  $\text{cm}^{-1}$  after ammonia adsorption for Cu-SSZ-13 are assigned to O–H stretching vibrations from Brønsted

acid sites (–Al–O(H)–Si–) in the zeolite framework, respectively (Fig. 3a). An analogous trend is observed for the Cu-ZSM-5 and Cu-BEA samples (Fig. 3a) for the O–H stretching vibrations from Brønsted acid sites with the values at 3604 and 3606  $\text{cm}^{-1}$ , respectively. The results indicate two types of Brønsted acid sites for Cu-SSZ-13 and one type for Cu-ZSM-5 and Cu-BEA.

Another type of OH group can appear at wavenumbers above 3700  $\text{cm}^{-1}$ , which are attributed to O–H stretching vibrations of Al (OH) or Si (OH) surface species.<sup>35,40</sup> The evolution of negative bands at 3736  $\text{cm}^{-1}$  for Cu-SSZ-13 and 3743  $\text{cm}^{-1}$  for Cu-ZSM-5 and 3732 and 3747  $\text{cm}^{-1}$  for Cu-BEA samples upon exposure to  $\text{NH}_3$  can be attributed to the adsorption of  $\text{NH}_3$  on Si–OH groups.<sup>35</sup> Hence, both surface silanol and structural OH groups in the zeolite framework are consumed or blocked by the adsorption of ammonia.<sup>40,41</sup> The other bands at 3780, 3779, and 3778  $\text{cm}^{-1}$  for Cu-SSZ-13, Cu-ZSM-5, and Cu-BEA, respectively, are related to adsorption of  $\text{NH}_3$  on Al (OH) sites.<sup>42</sup>

Another group of positive bands observed at 3186 and 3383  $\text{cm}^{-1}$  in the N–H stretching region (Fig. 3b) and positive bands at 1624 and 1263  $\text{cm}^{-1}$  in the N–H bending region (Fig. 3c), can be attributed to ammonia coordinated to Lewis acid sites (copper ions),<sup>43,44</sup> while the peaks at 3275 and 1454  $\text{cm}^{-1}$  features  $\text{NH}_4^+$  species adsorbed on Brønsted acid sites.<sup>39,45–47</sup> Hence, the peaks that are attributed to the same ammonia species, during  $\text{NH}_3$  addition, should represent the same trend of increasing or decreasing intensities of related peaks. This implies that while the intensities of the peaks in the N–H stretching region increase over time, the peaks related to N–H bending vibrations should also show an increasing trend (see Fig. S6†). In addition, the peaks at 2152, 2183, 1624, and 1570  $\text{cm}^{-1}$  (Fig. S6†) decrease by the introduction of ammonia, which can be due to that surface  $\text{NO}_x$  species mainly is formed on Brønsted acid sites where  $\text{NH}_3$  likely adsorbs strongly and can form  $\text{NH}_4^+$  ions and alternatively also can be due to the reaction between NO species and ammonia.<sup>46</sup> Simultaneously, adsorbed ammonia species are observed in the N–H stretching vibration region, at 3365 and 3274  $\text{cm}^{-1}$  for Cu-ZSM-5 and at 3356 and 3280  $\text{cm}^{-1}$  for Cu-BEA. Furthermore, adsorbed ammonia visible as peaks at 3192 and 3190  $\text{cm}^{-1}$ , for Cu-ZSM-5 and Cu-BEA, respectively are formed. In the N–H bending region, the peaks at 1466 and 1474  $\text{cm}^{-1}$  for Cu-ZSM-5 and Cu-BEA, respectively, attributed to ammonium ions adsorbed on Brønsted acid sites and the emerged peaks at 1622  $\text{cm}^{-1}$  for Cu-ZSM-5 and Cu-BEA attributed to ammonium ions adsorbed on Lewis acidic sites (see Fig. S6†). Comparing the results for the small- to large-pore zeolites at high temperatures shows that the intensity of the peaks related to nitrate and nitrite species is lower in the large-pore zeolite, which can be due to the lower stability of nitrate and ammonia species in the large-pore zeolites compared to medium and small-pore zeolites. The values for the peak intensity for nitrate species (around 1624  $\text{cm}^{-1}$ ), are shown in S3(b).†



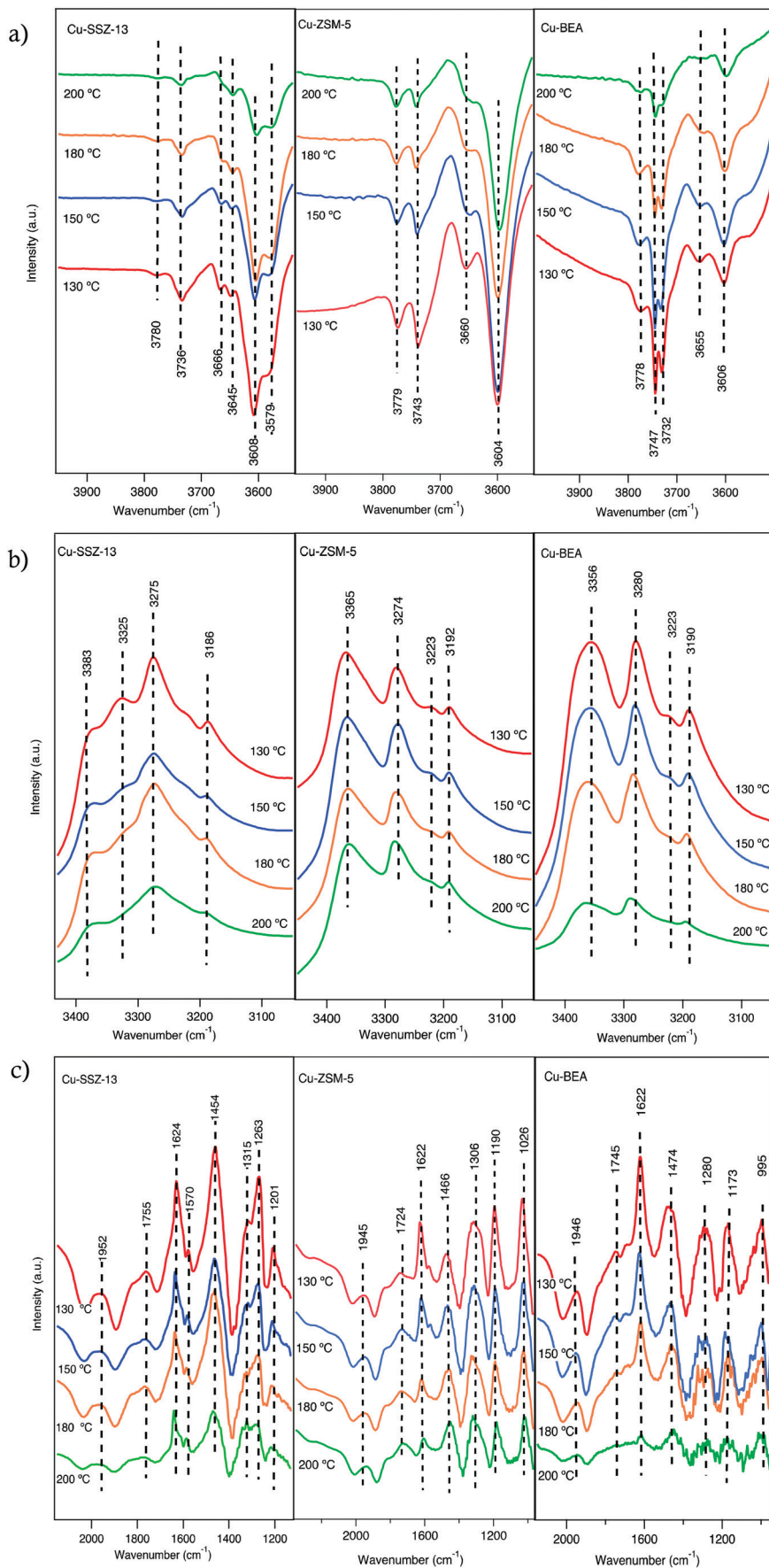


**Fig. 3** *In situ* DRIFT spectra after exposing the Cu-SSZ-13, Cu-ZSM-5 and Cu-BEA samples to 400 ppm NO, 400 ppm NH<sub>3</sub> and 10% O<sub>2</sub> for 15 min at 200, 180, 150 and 130 °C. The fig. (a–c) show different wavenumber regions.





Ma *et al.*<sup>48</sup> investigated  $\text{NH}_3$ -SCR over Cu-SSZ-13 and Cu-SAPO-34 and attributed absorption bands at 1493 and 1449  $\text{cm}^{-1}$  to N–H bending vibrations of  $\text{NH}_4^+$  on Brønsted acid sites. In addition, bands at 1617 and 1270  $\text{cm}^{-1}$  were assigned to N–H bending vibrations of  $\text{NH}_3$  adsorbed on Lewis acid sites. Also,  $\text{NH}_3$ -SCR over zeolites has been studied by Simons *et al.*,<sup>49</sup> and almost the same observations of the vibrational bands at 1450 and 1610  $\text{cm}^{-1}$  were reported. They recognized that the band at 1450  $\text{cm}^{-1}$  is the most pronounced signal of the whole spectra and corresponds to deformation vibrations of  $\text{NH}_4^+$  as  $\text{NH}_3$  species are bonded to the Brønsted acid sites by the formation of  $\text{NH}_4^+$ . The band at 1610  $\text{cm}^{-1}$  is attributed to N–H bending vibrations of ammonia on Lewis acid sites. These Lewis acid sites can either be related to the transition metal ions exchanged into the porous structure of the zeolite<sup>50</sup> or can originate from Al species located at the external surface of the zeolite.<sup>35,40,50,51</sup> In addition, Simons *et al.*<sup>49</sup> proposed that broadband at 2700–2300  $\text{cm}^{-1}$  is owing to stretching vibrations of weakly adsorbed ammonia that is not bonded directly to the acidic centers of the zeolite's lattice but alternatively attached to the strongly bonded ammonia as a secondary coordination layer.

Comparing the spectra for the samples exposed to standard SCR conditions at four different temperatures (Fig. 3a), reveals a trend with increasing intensity for the peaks in the O–H stretching region with decreasing temperature. Furthermore, for Cu-SSZ-13, the intensity of the IR bands for adsorbed  $\text{NH}_3$  at 1624  $\text{cm}^{-1}$  (Fig. 3c) diminishes at 200 °C, while the peak at 1454  $\text{cm}^{-1}$  (Fig. 3c), assigned to  $\text{NH}_4^+$  ions, is still detectable at this temperature. Hence, it can be concluded that at high temperatures, the  $\text{NH}_4^+$  ions are far more stable on Brønsted acid sites (–Al–O(H)–Si–) than on the Lewis acid sites (copper ions). Compared to Cu-SSZ-13, similar trends for ammonia adsorption are also observed during the adsorption process on Cu-ZSM-5 and Cu-BEA up to 180 °C, whereas a further increase in the temperature results in the disappearance of these two peaks. These results indicate that the ammonia-derived species adsorbed on Cu-ZSM-5 and Cu-BEA correspond to the adsorbed species on Cu-SSZ-13. Similarly, as for Cu-SSZ-13, ammonia adsorbs on both Lewis and Brønsted acidic sites in Cu-ZSM-5 and Cu-BEA, however, ammonia is less stable on Lewis acidic sites than on Brønsted acid sites and desorbs easily at 200 °C.<sup>45</sup> It is important to emphasize that the SCR reaction is complex in terms of reaction stoichiometry, as three reactants need to be activated and the nature of the catalytically active Cu species is crucial. From the low- to high-temperature reaction regimes,<sup>24,52</sup> the intensity of the peaks in the O–H stretching region decreases with increasing temperature between 130 and 200 °C which demonstrates the temperature dependency of the nature of the active Cu sites. The  $\text{NH}_3$ -SCR reaction advances through reduction and oxidation steps.<sup>53</sup> Copper ions are reduced from Cu(II) to Cu(I), while Cu(I) is reoxidized to Cu(II) in the reduction and oxidation step, respectively. It has been shown that under standard  $\text{NH}_3$ -SCR reaction conditions at low temperatures, the Cu ions are solvated by

$\text{NH}_3$ .<sup>54–56</sup> Two  $\text{NH}_3$  ligands are needed for the solvation of Cu(I) forming a linear  $\text{Cu}(\text{NH}_3)_2^+$  complex, while for Cu(II) several types of four-fold coordinated complexes can form, such as  $\text{Cu}(\text{NH}_3)_4^{2+}$ ,  $\text{Cu}(\text{OH})(\text{NH}_3)_3^+$ , and complexes containing a mixture of  $\text{NH}_3$  and  $\text{NO}_x$  ligands.<sup>53,57</sup> Also, above 250 °C, Cu ions coordinated to oxygen in the zeolite framework.<sup>55</sup> Also, Gao *et al.*<sup>23</sup> demonstrate that at low temperatures, the involvement of two Cu sites is essential for the standard SCR reaction, and the SCR reaction rate varies roughly linearly with Brønsted acid density. Furthermore, it should be considered that,  $\text{O}_2$  dissociation is an essential step in the  $\text{NH}_3$ -SCR reaction,<sup>52,54,58</sup> and its adsorption is advanced owing to the presence of  $\text{Cu}(\text{NH}_3)_2^+$  pairs.<sup>53,59</sup> It is proposed that, in the  $\text{NH}_3$ -SCR reaction first  $\text{O}_2$  is adsorbed on the surface and prior to the  $\text{NH}_3$  adsorption step, NO is adsorbed on the surface of zeolite as  $\text{NO}^+$ , and the activation of the  $\text{NH}_3$  molecule occurs by its coordination to  $\text{NO}^+$ , and the proton in the N–H bond is conveyed to oxygen to form an  $\text{OH}^-$  and a nitrosamide ( $\text{H}_2\text{NNO}$ ) species. Two nitrosamide species desorb from the Cu sites and decompose on Brønsted acid sites to form  $\text{N}_2$  and  $\text{H}_2\text{O}$ .  $\text{NO}^+$  is formed by adsorption of NO on the  $\text{Cu}^{2+}$  sites and through the reduction of Cu(II) to Cu(I). During the  $\text{NH}_3$ -SCR reaction, HONO can form and react with gas-phase  $\text{NH}_3$  and form an ammonium nitrite complex, which subsequently can decompose to  $\text{N}_2$  and  $\text{H}_2\text{O}$ . Another HONO species can form on the  $\text{Cu}^+$  site where  $\text{NO}^+$  and  $\text{OH}^-$  already are absorbed. Coordination of an  $\text{NH}_3$  molecule to the  $\text{NO}^+$  species results in the formation of HONO and  $\text{H}_2\text{NNO}$  species due to the transfer of a proton to the nitrite species.<sup>53</sup>

Upon the addition of  $\text{NO}_2$  (200 ppm) to the inlet gas composition (Fig. 4), a decreasing intensity trend appears for the peaks in both N–H stretching and bending vibration region over time, which indicates that  $\text{NO}_2$  consumes accumulated  $\text{NH}_3$  from the previous standard SCR reaction step, *i.e.*, indicating a higher reactivity of  $\text{NO}_2$  compared to NO.

A distinct rate of  $\text{NH}_3$  consumption is seen for species adsorbed on both Lewis and Brønsted acid sites in the series of DRIFT spectra. The intensity of the peak related to  $\text{NH}_3$  species adsorbed on the copper sites at 1623  $\text{cm}^{-1}$  decreases with time after the exposure to  $\text{NO}_2$ . On the other hand, the band at 1452  $\text{cm}^{-1}$ , indicating  $\text{NH}_3$  adsorbed on Brønsted acid sites, does not decrease in intensity to a large extent. While  $\text{NH}_3$  on Lewis acid sites is consumed by  $\text{NO}_2$ , nitrate species start to form on Lewis acid sites by the interactions with  $\text{NO}_2$ . According to the DRIFTS results for all three samples, it can be seen that the trend with decreasing intensity of the peaks related to the  $\text{NH}_3$  species is more pronounced for the large-pore zeolite compared to the medium and small-pore ones. This indicates that  $\text{NO}_2$  consumes  $\text{NH}_3$ , accumulated in the previous step of the experiment and the degree of consumption seems to be connected to the framework of the zeolite. It can be assumed that small and medium pore-zeolite accumulates more ammonia in its cages compared to large-pore zeolite, and the



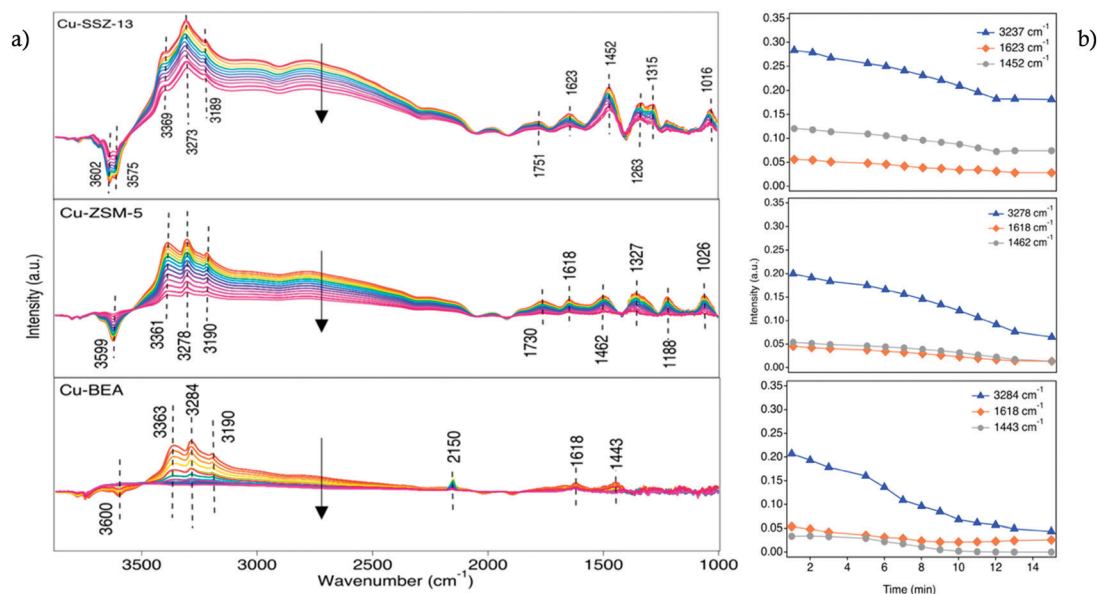


Fig. 4 a) *In situ* DRIFT spectra during exposure of the Cu-SSZ-13, Cu-ZSM-5, and Cu-BEA samples to 200 ppm NO, 200 ppm NO<sub>2</sub> and 10% O<sub>2</sub> at 200 °C, b) the intensity of three different peaks *versus* time.

consumption of trapped ammonia needs a higher amount of NO<sub>2</sub> and a longer reaction time. On the other hand, the intensity of the peaks at the N–H stretching region for the Cu-BEA sample decreases to almost zero within the same reaction time, which can be due to the less amount of ammonia trapped in large cages and consequently its faster consumption compared to other two zeolites. Chen *et al.*<sup>7</sup> reported that the formation of NO<sup>+</sup> decreases with time upon exposure to NO<sub>2</sub> and O<sub>2</sub> and it has been revealed that after 6 minutes of exposure, the intensity of the NO<sup>+</sup> peak decreased to about 2/3 of its initial size. Also, at the same time, the intensity of the peaks related to nitrate species increased slightly. Also, Zhu *et al.*<sup>60</sup> observed that under fast NH<sub>3</sub>-SCR reaction conditions, the various reactivity of NH<sub>4</sub>NO<sub>3</sub> with NO leads to the distinguished NO<sub>2</sub> effects on N<sub>2</sub>O formation

for Cu-SSZ-13 and Cu-SSZ-39. For instance, for Cu-SSZ-13, the slow reaction between NH<sub>4</sub>NO<sub>3</sub> and NO results in accumulation of NH<sub>4</sub>NO<sub>3</sub> and blocking of the pores of the zeolite, and subsequently inhibition of the SCR activity by NO<sub>2</sub>.

These results are in agreement with NH<sub>3</sub>-TPD experiments carried out in the flow reactor to quantify the NH<sub>3</sub> storage (data reported in our recent publication).<sup>61</sup> From the integrated peak area of TPD profiles, it is observed that the NH<sub>3</sub> storage is roughly in the same range for Cu-SSZ-13 (0.756 mmol g<sup>−1</sup>) and Cu-ZSM-5 (0.791 mmol g<sup>−1</sup>) followed by Cu-BEA (0.626 mmol g<sup>−1</sup>). Based on the discussed DRIFTS results in Fig. 3), it is clear that in the Cu-SSZ-13 and Cu-ZSM-5 samples, NH<sub>3</sub> is strongly bonded to the OH Brønsted acid sites rather than to the silanol groups, but in the case of

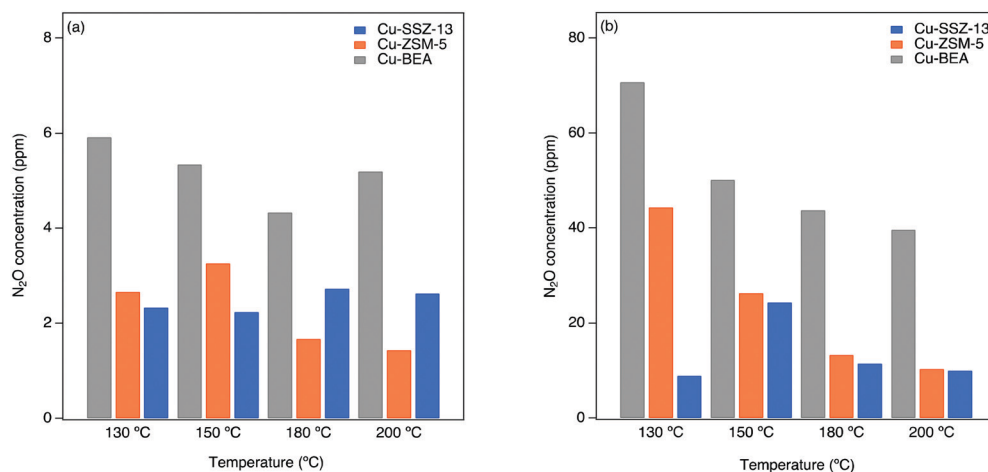


Fig. 5 N<sub>2</sub>O concentration as a function of catalyst temperature within a) standard (400 ppm NO, 400 ppm NH<sub>3</sub>, 10% O<sub>2</sub>) and b) fast SCR (200 ppm NO, 200 ppm NO<sub>2</sub>, 400 ppm NH<sub>3</sub>, 10% O<sub>2</sub>) reaction over Cu-based zeolites.



Cu-BEA  $\text{NH}_3$  is mainly bonded weakly to silanol groups. This facilitates  $\text{NH}_3$  consumption with  $\text{NO}_2$  in large-pore zeolites and results in a fast-decreasing trend in N–H stretching and bending region compared to medium- and small-pore zeolites.

### 3.3. Formation of $\text{N}_2\text{O}$ during standard and fast SCR reaction conditions

The  $\text{N}_2\text{O}$  formation is evaluated by kinetic tests in the flow reactor during both standard and fast SCR reaction conditions (original data are shown in our previous work).<sup>61</sup>

Further details regarding the experimental descriptions are given in section 2.3.

In Fig. 5, the  $\text{N}_2\text{O}$  concentration is shown as a function of catalyst temperature for Cu-SSZ-13, Cu-ZSM-5, and Cu-BEA during both standard and fast SCR reaction conditions at 130, 150, 180, and 200 °C. The results reveal a clear trend for low and high temperatures. As can be seen, the  $\text{N}_2\text{O}$  formation is higher for Cu-BEA compared to Cu-ZSM-5 and Cu-SSZ-13 for the entire temperature range.

During fast SCR reaction conditions, the formation of  $\text{N}_2\text{O}$  is much higher for all samples compared to standard SCR reaction conditions. It is noteworthy that the

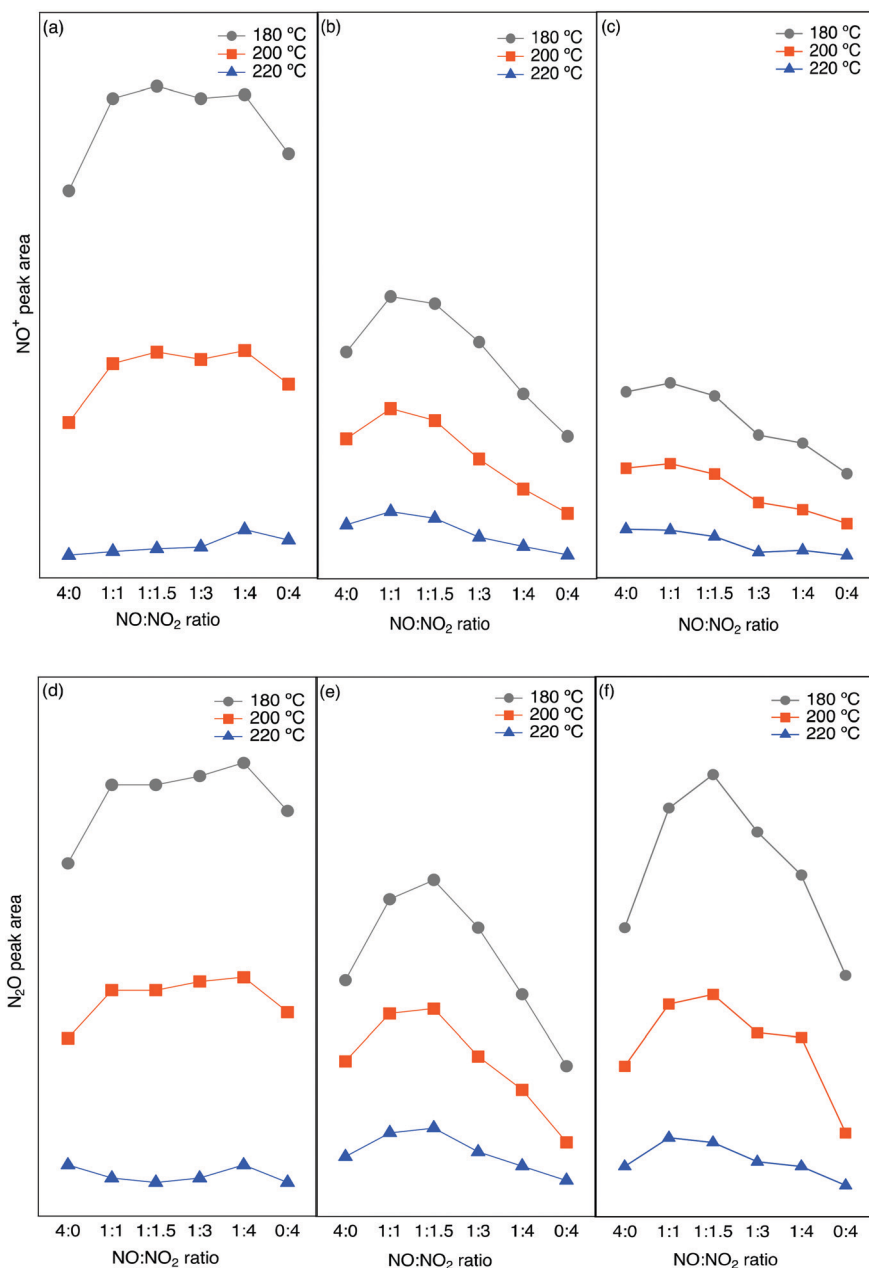


Fig. 6 Integrated peak area from *in situ* DRIFTS experiments for  $\text{NO}^+$  (a–c) and  $\text{N}_2\text{O}$  (d–f) for different  $\text{NO}/\text{NO}_2$  ratios at three different temperatures over (a and d) Cu-SSZ-13, (b and e) Cu-ZSM-5 and (c and f) Cu-BEA.



presence of  $\text{NO}_2$  has a considerable effect on the SCR activity at lower temperatures,<sup>1,62</sup> which is likely due to the higher activity of  $\text{NO}_2$  compared to  $\text{O}_2$  to reoxidize  $\text{Cu(I)}$  to  $\text{Cu(II)}$ . In Fig. 5, the highest amount of  $\text{N}_2\text{O}$  during fast SCR conditions is observed for Cu-BEA, followed by Cu-ZSM-5 and Cu-SSZ-13.

As mentioned earlier, the  $\text{N}_2\text{O}$  formation during the SCR reaction at 250–280 °C proceeds partly *via* the decomposition of  $\text{NH}_4\text{NO}_3$ , which is an intermediate formed on the zeolite when ammonia reacts with the surface nitrate species during  $\text{NH}_3$ -SCR reaction conditions.<sup>2,63,64</sup> It is also proposed by Lee *et al.*<sup>65</sup> that over Cu-ZSM-5 and Cu-SSZ-13 catalyst, the  $\text{N}_2\text{O}$  yield is due to the decomposition of  $\text{NH}_4\text{NO}_3$ . The same was also reported by Devadas *et al.*,<sup>66</sup> for low-temperature  $\text{N}_2\text{O}$  formation over Fe-ZSM-5. On the contrary, Feng *et al.*<sup>8</sup> recently proposed that  $\text{N}_2\text{O}$  formation at low temperatures over Cu-CHA is connected to  $\text{H}_2\text{NNO}$  decomposition over  $(\text{NH}_3)_2\text{Cu-OOH-Cu}(\text{NH}_3)_2$  complexes.

The ammonium nitrate (AN) TPD results over the samples indicate that AN has a shorter resistance time in large-pore zeolites, which results in a continuous decomposition of AN to  $\text{N}_2\text{O}$ .<sup>61</sup> These results are in agreement with the DRIFTS measurements during  $\text{NO}_2$  adsorption (step 5 in Table 1). As discussed in section 3.2, Fig. 4, for the large-pore zeolite all pre-adsorbed  $\text{NH}_3$  can be consumed by the introduced  $\text{NO}_2$ . This can lead to higher and faster AN formation and release during the SCR reaction and the formation of more  $\text{N}_2\text{O}$  by its decomposition. Furthermore, based on DRIFTS studies on NO oxidation (depicted in Fig. 2), at low temperatures, the nitrate/ $\text{NO}^+$  ratio is higher for Cu-BEA compared to Cu-ZSM-5 and Cu-SSZ-13.

### 3.4. Effect of $\text{NO}/\text{NO}_2$ ratio on the evolution of surface species

To investigate the effect of the  $\text{NO}/\text{NO}_2$  ratio on the formation of  $\text{N}_2\text{O}$ , a series of experiments was carried out at three different bed temperatures (220, 200, 180 °C) for the Cu-SSZ-13, Cu-ZSM-5, and Cu-BEA samples with varying  $\text{NO}/\text{NO}_2$  ratio from 4:0, 1:1, 1:1.5, 1:3, 1:4 to 0:4. The results for the integrated peak area of  $\text{N}_2\text{O}$  ( $2237\text{ cm}^{-1}$  with a shoulder at  $2208\text{ cm}^{-1}$ ) and  $\text{NO}^+$  ( $2150\text{ cm}^{-1}$ ) species at the steady-state of the reaction are shown in Fig. 6. The peak position for  $\text{N}_2\text{O}$  has been measured by DRIFTS on both KBr and diamond powder and compared with the gas phase  $\text{N}_2\text{O}$  obtained from Nist (the symmetric NN and NO stretch is at  $2202$  and  $1270\text{ cm}^{-1}$ , respectively).<sup>67</sup> The related spectra for the peak position of  $\text{N}_2\text{O}$  are shown in Fig. S10.† Based on the obtained results from related peak integration (original spectra are shown in Fig. S9(a–c)†), even though there is  $\text{N}_2\text{O}$  formation in the presence of only NO or  $\text{NO}_2$ , it is clear that for higher  $\text{N}_2\text{O}$  formation the presence of both NO and  $\text{NO}_2$  is required. It is also obvious from reactor studies (data is shown in section 3.3) that a higher amount of  $\text{N}_2\text{O}$  is formed during the fast SCR reaction conditions compared to standard SCR.

The integrated  $\text{N}_2\text{O}$  and  $\text{NO}^+$  peak area are plotted as a function of the  $\text{NO}/\text{NO}_2$  ratio, and it clearly shows a higher peak area for the small-pore zeolite sample compared to the other two samples. Comparing the  $\text{N}_2\text{O}$  peak area for the three samples shows that for the small-pore Cu-SSZ-13 sample, at all three temperatures the  $\text{N}_2\text{O}$  peak area gradually increases from  $\text{NO}/\text{NO}_2 = 0:4$  to  $1:4$  and decreases again, while for the medium (Cu-ZSM-5) and large-pore (Cu-BEA) samples the  $\text{N}_2\text{O}$  peak area reaches a maximum at  $\text{NO}/\text{NO}_2 = 1:1.5$ . A further increase in the  $\text{NO}/\text{NO}_2$  ratio results in a decline in  $\text{N}_2\text{O}$  formation for the catalysts. The same trend is seen for the Cu-ZSM-5 and Cu-BEA samples at all three temperatures. Furthermore, the highest value for the  $\text{NO}^+$  peak area for Cu-SSZ-13 appears at a  $\text{NO}/\text{NO}_2$  ratio of  $1:1.5$ , whereas Cu-ZSM-5 and Cu-BEA show the highest peak area for the  $1:1$  ratio. At 180 °C, however,  $\text{N}_2\text{O}$  formation on Cu-SSZ-13 increases slightly when the  $\text{NO}/\text{NO}_2$  ratio increases from  $0:4$  to  $1:4$  and starts to decrease again at a higher ratio. For Cu-BEA, the value of  $\text{NO}^+$  reveals an increasing trend with an increased ratio. Almost the same trend can be seen for the  $\text{NO}^+$  peak as well, which can be due to the relation between the amount of  $\text{NO}^+$  and  $\text{N}_2\text{O}$  formation. For Cu-SSZ-13, at all temperatures, the peak area for  $\text{N}_2\text{O}$  formation is the highest at  $\text{NO}/\text{NO}_2$  ratio of  $1:4$ . For the other two zeolites, the highest amount is seen for the ratio of  $1:1$  for all three temperatures. Furthermore,  $\text{NO}^+$  and  $\text{N}_2\text{O}$  formation are higher at a lower temperature, which can be due to the coverage of  $\text{NO}^+$  that decreases with increasing temperature. Based on the study by Liu *et al.*<sup>68</sup> on the effect of  $\text{NO}_x$  ratio on the  $\text{N}_2\text{O}$  formation, the  $\text{N}_2\text{O}$  amount is different below and above 250 °C. Below 250 °C there should be maximum  $\text{N}_2\text{O}$  formation with less  $\text{NO}_2$  as is in line with our study. The reason for this can be the formation of a higher amount of ammonium nitrate with high  $\text{NO}_2$  concentration and consequently blocking of the surface, which results in lower conversion and thereby a lower  $\text{N}_2\text{O}$  formation. At higher temperatures, no surface blocking occurs and the maximum  $\text{N}_2\text{O}$  formation is achieved for 100%  $\text{NO}_2$ .

The integrated peak area attributed to nitrate species ( $1530\text{--}1700\text{ cm}^{-1}$ ) has been plotted *versus* the  $\text{NO}/\text{NO}_2$  ratio in Fig. 7. A similar trend is seen for all three zeolites, with the highest value of nitrate species at low temperature and low  $\text{NO}_2$  concentrations. At an  $\text{NO}/\text{NO}_2$  ratio of  $4:0$ , which is the standard SCR reaction condition, the highest peak area can be related to the lower reaction rate. On the other hand, by the addition of  $\text{NO}_2$  with a  $\text{NO}/\text{NO}_2$  ratio of  $1:1$ , the fast SCR reaction proceeds, consuming the surface nitrate species giving rise to a decrease in the related peak area.

The addition of more  $\text{NO}_2$  gradually increases the related peak area. This is in line with the lowest amount of  $\text{NO}^+$  and  $\text{N}_2\text{O}$  formation when we have the highest nitrate species.

In summary, the zeolite framework structure and reaction temperature have an influence on the formation of undesired by-products during ammonia-SCR of  $\text{NO}_x$ . The results from DRIFTS and flow reactor experiments reveal that  $\text{NO}^+$  and





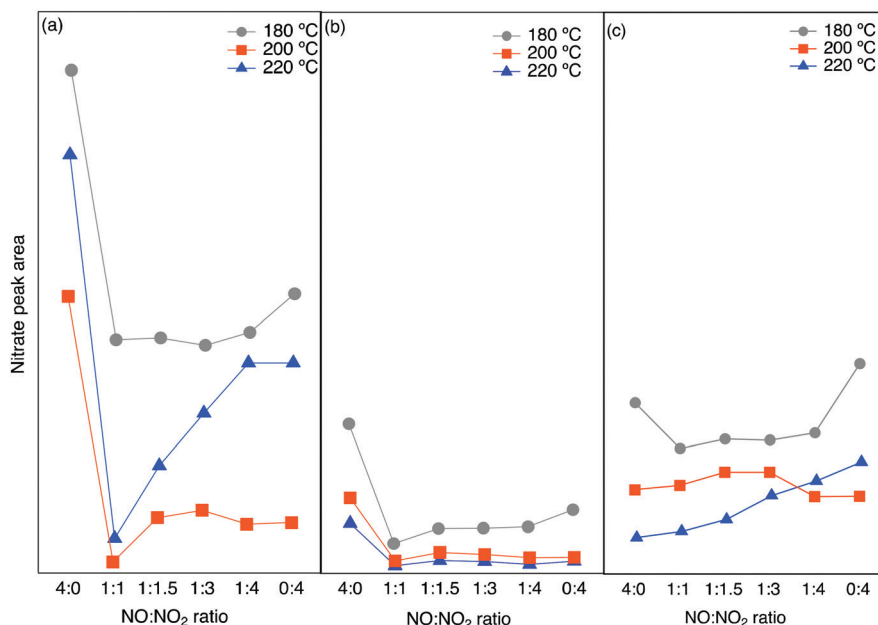


Fig. 7 Integrated peak area from *in situ* DRIFTS experiments for nitrate species for different NO/NO<sub>2</sub> ratios at three different temperatures over a) Cu-SSZ-13, b) Cu-ZSM-5 and c) Cu-BEA.

nitrate species are the major surface species during NO oxidation. Evaluating the effect of various NO<sub>x</sub>-ratio shows the higher formation of NO<sup>+</sup> and N<sub>2</sub>O species at lower temperatures and higher N<sub>2</sub>O formation for the large-pore zeolite (Cu-BEA) compared to medium- (Cu-ZSM-5) and small-pore (Cu-SSZ-13), based on the results from DRIFTS studies and flow reactor experiments.

### 3.5. DFT calculations

DFT calculations were performed to assist the assignments of DRIFTS results. Among the three studied zeolites, SSZ-13 has emerged as the preferred system for NH<sub>3</sub>-SCR and is, therefore, considered in the DFT calculations.

To obtain a reference, the wavenumber of the N–O stretch vibration for NO and NO<sup>+</sup> in the gas phase was calculated, resulting in 1923 and 2405 cm<sup>−1</sup>, respectively. The calculated wavenumbers are higher than the experimental corresponding values by a factor of 1.03, which is consistent with previous DFT studies using the same approach.<sup>69</sup>

Previous work suggests that the peak at 2156 cm<sup>−1</sup> should be attributed to the N–O stretching vibration of NO<sup>+</sup> adsorbed on Lewis acid sites.<sup>9</sup> However, Hadjiivanov *et al.*<sup>33</sup> assign a peak at 2132 cm<sup>−1</sup> to NO adsorbed on H-ZSM-5. As

the relationship between the NO wavenumber and the adsorption site remains unclear, the wavenumber of N–O stretching vibration of NO on potential sites in SSZ-13 was calculated, see Fig. 9. NO adsorbed at Lewis acid site has an adsorption energy of 0.6 eV and a stretching vibration at 1926 cm<sup>−1</sup>, which indicates that NO at this adsorption site is neutral. However, when NO occupies Al–Lewis acid sites (O–Al–O), the wavenumber is shifted to 2060 cm<sup>−1</sup> and the adsorption energy is increased to 0.81 eV. As a comparison, NO adsorption over SSZ-13 in the absence of Cu-sites was also investigated. There are four types of Brønsted acid sites in SSZ-13 with one Al on the six-membered ring. The structure is shown in Fig. 8. The adsorption energy for NO adsorbed on the different sites, is high and similar, being

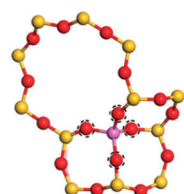


Fig. 8 Four types of Brønsted acid sites in SSZ-13.

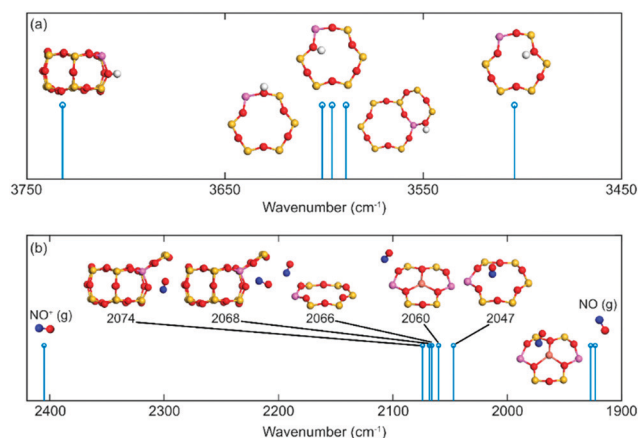


Fig. 9 Simulated vibrations for (a) O–H and (b) N–O on different CHA sites. Atomic color codes: H (white), N (blue), O (red), Al (pink), and Si (yellow).



about 2 eV (within 0.1 eV) and the wavenumber for the stretching vibration is in the range from 2047 to 2074  $\text{cm}^{-1}$ . Comparing the results for NO and  $\text{NO}^+$  in the gas phase indicates that the peak around 2150  $\text{cm}^{-1}$  should be associated with NO adsorbed on Cu-Lewis acid sites ( $\text{Cu}^{2+}$ ). Moreover, the similar adsorption energies and slightly different frequencies for NO adsorbed on Al-Lewis acid sites (O–Al–O) close to the Cu-Lewis sites could explain the double absorption peaks in the DRIFT spectra (Fig. 1).

The negative peaks after ammonia adsorption in the high wavenumbers region shown in Fig. 3(a) were considered to originate from O–H stretching vibrations from Brønsted acid sites in the zeolite framework. It is noteworthy that SSZ-13 has a more complex multiple peak profile than the other two zeolites. Thus, the O–H frequency of H on different sites has been calculated to compare with the experimental results. The data indicate that the position of the stretching vibration for O–H depends on the adsorption site. O–H stretching vibrations of Si (OH) gives a relatively low wavenumber (3504  $\text{cm}^{-1}$ ), whereas the Al (OH) surface species results in a wavenumber at about 3600  $\text{cm}^{-1}$ . The highest calculated wavenumber of O–H on Brønsted acid sites is 3732  $\text{cm}^{-1}$ . Al (OH) is the preferred adsorption site with adsorption energy that is about 0.7 eV higher than Si (OH). This is probably the reason why the measured wavenumber is concentrated mainly at 3579 and 3608  $\text{cm}^{-1}$ .

The DRIFTS results indicate that nitrate species are the main product formed during the NO oxidation step, which contributed to the peak at about 1620  $\text{cm}^{-1}$ , being the N–O stretching vibrations of surface nitrate species. It is

noteworthy that this peak appears independently of whether ammonia is present or not in all three zeolites. To study this, the IR spectra of framework nitrate ( $[\text{CuNO}_3]^+$ ) and mobile nitrate species ( $[\text{Cu}(\text{NH}_3)_2\text{NO}_3]^+$ ) have been calculated (Fig. 10). Both cases show a peak of 1604  $\text{cm}^{-1}$  which is associated with a O–N stretching vibrations in  $\text{NO}_3^-$ . This result is an illustration of the 1620 and 1624  $\text{cm}^{-1}$  peaks of Cu-SSZ-13 in Fig. 1 and 3.

Previous spectroscopy and first-principles calculations have demonstrated that Cu(I) is preferably present in the form of linear  $\text{Cu}(\text{NH}_3)_2^+$  under low-temperature SCR reaction conditions. The linear complex has also been proven to be a critical site for  $\text{O}_2$  activation by forming Cu-peroxo ( $[\text{Cu}_2(\text{NH}_3)_4(\text{O}_2)]^{2+}$ ). In the recent work of Negri *et al.*,<sup>70</sup> the strong adsorption of extra  $\text{NH}_3$  on Cu-peroxo has been reported. Based on the measurement conditions, we calculated the IR spectra of  $[\text{Cu}_2(\text{NH}_3)_5(\text{O}_2)]^{2+}$  complex for reference. The stretching vibrations of the N–H bond are in the 3283 to 3484  $\text{cm}^{-1}$  range, whereas the bending wavenumbers are between 1589 to 1638  $\text{cm}^{-1}$  and 1213 to 1272  $\text{cm}^{-1}$ , respectively. These peaks are consistent with the measurements.<sup>43,44</sup> The DFT calculations of  $\text{NH}_3$  adsorption on Brønsted acid sites ( $\text{NH}_4^+$ ) shows high-intensity signatures at 3191, 2512, and 1492  $\text{cm}^{-1}$ , which are in good agreement with the DRIFTS results in Fig. S8.†

## 4. Conclusions

The influence of the zeolite framework structure on the formation of  $\text{N}_2\text{O}$  during ammonia SCR of  $\text{NO}_x$  has been studied for three different zeolite samples with varying framework structures: Cu-SSZ-13 (CHA), Cu-ZSM-5 (MFI), and Cu-BEA (BEA). The results show that the formation of  $\text{N}_2\text{O}$  is closely connected with the structure of the zeolite, feed gas composition, and temperature. At lower temperatures, the formation of  $\text{NO}^+$  species is higher for the Cu-SSZ-13, Cu-ZSM-5, and Cu-BEA samples and starts to decrease when increasing the temperature to 200 °C. In addition, comparing the intensity ratio of nitrate or nitrite/ $\text{NO}^+$  for the samples at different temperatures reveals that at low temperature, this value is higher for Cu-BEA compared to the two other zeolites, which decreases by increasing temperature. This can be owing to the higher stabilization of  $\text{NO}^+$  in the small-pore zeolite than in the zeolites with medium and large-pores at low temperatures. Furthermore, by adding  $\text{NH}_3$ , *i.e.*, resulting in standard SCR reaction, absorption peaks corresponding to N–H stretching and bending vibrations appear, and at the same time, negative peaks appear in the O–H stretching region, indicating blocking/replacement of surface OH-groups by  $\text{NH}_3$ . Interestingly, when  $\text{NH}_3$  is removed and  $\text{NO}_2$  is added to the feed, the N–H stretching and bending vibrations show a trend with decreasing intensity, with the decrease being more pronounced for increasing pore size. It is likely that ammonia surface species, accumulated during the previous step, are consumed by  $\text{NO}_2$  and the degree of consumption seems to be related to the framework of the

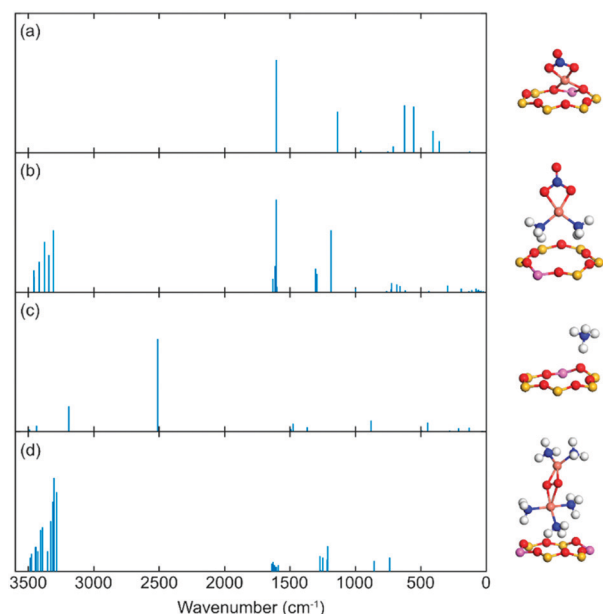


**Fig. 10** Simulated IR vibrations for different species adsorbed on different Cu-CHA and CHA sites. (a)  $[\text{CuNO}_3]^+$  complex, (b)  $[\text{Cu}(\text{NH}_3)_2\text{NO}_3]^+$  complex, (c)  $\text{NH}_4^+$ , and (d)  $[\text{Cu}_2(\text{NH}_3)_5(\text{O}_2)]^{2+}$  complex. Atomic colour codes: H (white), N (blue), O (red), Al (pink), Si (yellow) and Cu (bronze).



zeolite. Also, the weakly bonded  $\text{NH}_3$  on silanol groups in Cu-BEA accelerates its consumption by adding  $\text{NO}_2$  and can be the result of a higher intensity decrease in the N–H stretching and bending vibration region compared to the other two zeolite samples. Additional experiments with the Cu-based zeolites, at different  $\text{NO}/\text{NO}_2$  ratios during SCR reaction conditions show that the presence of both  $\text{NO}$  and  $\text{NO}_2$  is essential for  $\text{N}_2\text{O}$  formation, with the highest formation for an  $\text{NO}/\text{NO}_2$  ratio of 1 : 1. Based on the obtained results, it can be concluded that both reaction temperature and framework structure of the zeolite have a direct influence on the  $\text{N}_2\text{O}$  formation. The results from both DRIFTS studies and flow reactor experiments illustrate higher  $\text{N}_2\text{O}$  formation for the large-pore zeolite compared to medium- and small-pore zeolites. At low temperatures, this can be due to a higher formation of ammonium nitrate over the Cu-BEA zeolite and its subsequent decomposition to  $\text{N}_2\text{O}$ .

In addition, density functional theory calculations for Cu-SSZ-13 and H-SSZ-13 reveals that  $\text{NO}$  can be adsorbed at different Al–O–Al sites with similar adsorption energies and N–O stretching vibrations, which rationalizes the emergence of the double absorption peaks in the DRIFT spectrum. Furthermore, in the O–H stretching region, a low wavenumber is observed for Si (OH) compared to the value for Al (OH) surface species. Also, simulating the IR spectra of the DRIFTS results for mobile nitrate species and framework nitrate provides a peak around  $1604\text{ cm}^{-1}$  attributed to the O–N bond in  $\text{NO}_3^-$ . In general, the  $\text{N}_2\text{O}$  formation during the  $\text{NH}_3$ -SCR reaction depends on the emergence of various intermediates, and the surface species and follows different mechanistic pathways at low and high temperatures. It seems that adsorbed  $\text{NO}$  and formed nitrate species during  $\text{NO}$  oxidation can be two of the main contributors and initiators for the  $\text{N}_2\text{O}$  formation and it seems that both Cu-Lewis ( $\text{Cu}^{2+}$ ) and Al-Lewis (Al–O–Al) sites can provide adsorption sites for the formed  $\text{NO}^+$ .

## Author contributions

Ghodsieh Isapour: investigation – conducting a research and investigation process, specifically performing the experiments, or data/evidence collection. Visualization – preparation, creation, and/or presentation of the published work, specifically visualization/data presentation. Writing the original draft – preparation, creation, and/or presentation of the published work, specifically writing the initial draft (including substantive translation). Aiyong Wang: conceptualization – ideas; formulation or evolution of overarching research goals and aims. Joonsoo Han: investigation – conducting a research and investigation process, specifically performing the experiments, or data/evidence collection for the flow reactor section. Yingxin Feng: formal analysis – application of statistical, mathematical, computational, or other formal techniques to analyze or synthesize study data. Writing the original draft – writing the

initial draft for the DFT calculation section. Henrik Grönbeck: conceptualization – ideas; formulation or evolution of overarching research goals and aims. Derek Creaser: conceptualization – ideas; formulation or evolution of overarching research goals and aims. Louise Olsson: conceptualization – ideas; formulation or evolution of overarching research goals and aims. Magnus Skoglundh: conceptualization – ideas; formulation or evolution of overarching research goals and aims. Supervision – oversight and leadership responsibility for the research activity planning and execution, including mentorship external to the core team. Hanna Härelind: conceptualization – ideas; formulation or evolution of overarching research goals and aims. Supervision – oversight and leadership responsibility for the research activity planning and execution, including mentorship external to the core team.

## Conflicts of interest

There are no conflicts to declare.

## Acknowledgements

This work has been performed within the Competence Centre for Catalysis, which is hosted by the Chalmers University of Technology and financially supported by the Swedish Energy Agency, Chalmers, and the member companies; AB Volvo, ECAPS AB, Johnson Matthey AB, Preem AB, Scania CV AB, and Umicore Denmark ApS. The calculations have been performed at C3SE (Göteborg) through a SNIC grant and additional financial support was obtained from the Swedish Energy Agency project 47110-1.

## Notes and references

- 1 H. Kubota, C. Liu, T. Toyao, Z. Maeno, M. Ogura, N. Nakazawa, S. Inagaki, Y. Kubota and K. I. Shimizu, *ACS Catal.*, 2020, **10**, 2334–2344.
- 2 D. Zhang and R. T. Yang, *Energy Fuels*, 2018, **32**, 2170–2182.
- 3 M. J. Kim, S. J. Lee, I. S. Ryu, M. W. Jeon, S. H. Moon, H. S. Roh and S. G. Jeon, *Mol. Catal.*, 2017, **442**, 202–207.
- 4 T. Nobukawa, M. Yoshida, K. Okumura, K. Tomishige and K. Kunitomi, *J. Catal.*, 2005, **229**, 374–388.
- 5 J. Pérez-Ramírez, F. Kapteijn, K. Schöffel and J. A. Moulijn, *Appl. Catal., B*, 2003, **44**, 117–151.
- 6 K. Leistner, O. Mihai, K. Wijayanti, A. Kumar, K. Kamasamudram, N. W. Currier, A. Yezerets and L. Olsson, *Catal. Today*, 2015, **258**, 49–55.
- 7 H. Y. Chen, M. Kollar, Z. Wei, F. Gao, Y. Wang, J. Szanyi and C. H. F. Peden, *Catal. Today*, 2019, **320**, 61–71.
- 8 Y. Feng, T. V. W. Janssens, P. N. R. Vennestrom, J. Jansson, M. Skoglundh and H. Grönbeck, *J. Phys. Chem. C*, 2021, **125**(40), 21975–21987.
- 9 M. P. Ruggeri, I. Nova, E. Tronconi, J. A. Pihl, T. J. Toops and W. P. Partridge, *Appl. Catal., B*, 2015, **166–167**, 181–192.
- 10 H. Liu, C. You and H. Wang, *Chem. Eng. J.*, 2020, **382**, 122756.



- 11 M. Anstrom, N. Y. Topsøe and J. A. Dumesic, *J. Catal.*, 2003, **213**, 115–125.
- 12 G. Kresse and J. Hafner, *Phys. Rev. B: Condens. Matter Mater. Phys.*, 1993, **48**, 13115–13118.
- 13 G. Kresse and J. Hafner, *Phys. Rev. B: Condens. Matter Mater. Phys.*, 1994, **49**, 14251–14269.
- 14 R. A. Vargas-Hernández, *J. Phys. Chem. A*, 2020, **124**, 4053–4061.
- 15 G. Kresse and J. Furthmüller, *Comput. Mater. Sci.*, 1996, **6**, 15–50.
- 16 D. Joubert, *Phys. Rev. B: Condens. Matter Mater. Phys.*, 1999, **59**, 1758–1775.
- 17 P. E. Blöchl, *Phys. Rev. B: Condens. Matter Mater. Phys.*, 1994, **50**, 17953–17979.
- 18 J. P. Perdew, K. Burke and M. Ernzerhof, *Phys. Rev. Lett.*, 1996, **77**, 3865–3868.
- 19 S. Grimme, J. Antony, S. Ehrlich and H. Krieg, *J. Chem. Phys.*, 2010, **132**, 154104.
- 20 A. Allouche, *J. Comput. Chem.*, 2012, **32**, 174–182.
- 21 L. Y. Isseroff and E. A. Carter, *Phys. Rev. B: Condens. Matter Mater. Phys.*, 2012, **85**, 1–7.
- 22 D. Karhánek, *dakarhanek/VASP-infrared-intensities: VASP-infrared-intensities*, DOI: [10.5281/zenodo.3930989](https://doi.org/10.5281/zenodo.3930989).
- 23 F. Gao, N. M. Washton, Y. Wang, M. Kollár, J. Szanyi and C. H. F. Peden, *J. Catal.*, 2015, **331**, 25–38.
- 24 F. Gao, E. D. Walter, M. Kollar, Y. Wang, J. Szanyi and C. H. F. Peden, *J. Catal.*, 2014, **319**, 1–14.
- 25 C. Paolucci, A. A. Parekh, I. Khurana, J. R. Di Iorio, H. Li, J. D. Albarracin Caballero, A. J. Shih, T. Anggara, W. N. Delgass, J. T. Miller, F. H. Ribeiro, R. Gounder and W. F. Schneider, *J. Am. Chem. Soc.*, 2016, **138**, 6028–6048.
- 26 J. Liang, J. Su, Y. Wang, Z. Lin, W. Mu, H. Zheng, R. Zou, F. Liao and J. Lin, *Microporous Mesoporous Mater.*, 2014, **194**, 97–105.
- 27 X. Wang, A. Shishkin, F. Hemmingsson, M. Skoglundh, F. J. Martinez-Casado, L. Bock, A. Idström, L. Nordstierna, H. Härelind and P. A. Carlsson, *RSC Adv.*, 2018, **8**, 36369–36374.
- 28 Y. S. Ryou, J. Lee, S. J. Cho, H. Lee, C. H. Kim and D. H. Kim, *Appl. Catal., B*, 2017, **212**, 140–149.
- 29 S. K. Jesudoss, J. J. Vijaya, K. Kaviyarasu, L. J. Kennedy, R. Jothi Ramalingam and H. A. Al-Lohedan, *RSC Adv.*, 2018, **8**, 481–490.
- 30 A. R. Do Nascimento, G. P. De Figueredo, E. M. F. Silva, M. A. F. Melo, D. M. A. Melo and M. J. B. De Souza, *Rev. Virtual Quim.*, 2017, **9**, 1570–1582.
- 31 B. Chen, R. Xu, R. Zhang and N. Liu, *Environ. Sci. Technol.*, 2014, **48**, 13909–13916.
- 32 C. M. Chanquía, K. Sapag, E. Rodríguez-Castellón, E. R. Herrero and G. A. Eimer, *J. Phys. Chem. C*, 2010, **114**, 1481–1490.
- 33 K. Hadjiivanov, J. Saussey, J. L. Freysz and J. C. Lavalley, *Catal. Lett.*, 1998, **52**, 103–108.
- 34 J. H. Kwak, H. Zhu, J. H. Lee, C. H. F. Peden and J. Szanyi, *Chem. Commun.*, 2012, **48**, 4758–4760.
- 35 D. Wang, L. Zhang, K. Kamasamudram and W. S. Epling, *ACS Catal.*, 2013, **3**, 871–881.
- 36 M. P. Ruggeri, A. Grossale, I. Nova, E. Tronconi, H. Jirglova and Z. Sobalik, *Catal. Today*, 2012, **184**, 107–114.
- 37 A. Penkova, K. Hadjiivanov, M. Mihaylov, M. Daturi, J. Saussey and J. C. Lavalley, *Langmuir*, 2004, **20**, 5425–5431.
- 38 M. Iwasaki and H. Shinjoh, *Phys. Chem. Chem. Phys.*, 2010, **12**, 2365–2372.
- 39 H. Y. Chen, Z. Wei, M. Kollar, F. Gao, Y. Wang, J. Szanyi and C. H. F. Peden, *J. Catal.*, 2015, **329**, 490–498.
- 40 L. Wang, W. Li, G. Qi and D. Weng, *J. Catal.*, 2012, **289**, 21–29.
- 41 H. Zhu, J. H. Kwak, C. H. F. Peden and J. Szanyi, *Catal. Today*, 2013, **205**, 16–23.
- 42 R. Hajjar, Y. Millot, P. P. Man, M. Che and S. Dzwigaj, *J. Phys. Chem. C*, 2008, **112**, 20167–20175.
- 43 K. I. Hadjiivanov, *Catal. Rev.: Sci. Eng.*, 2000, **42**, 71–144.
- 44 F. Giordanino, P. N. R. Vennestrom, L. F. Lundegaard, F. N. Stappen, S. Mossin, P. Beato, S. Bordiga and C. Lamberti, *Dalton Trans.*, 2013, **42**, 12741–12761.
- 45 S. Elzey, A. Mubayi, S. C. Larsen and V. H. Grassian, *J. Mol. Catal. A: Chem.*, 2008, **285**, 48–57.
- 46 M. Wallin, C. J. Karlsson, A. Palmqvist and M. Skoglundh, *Top. Catal.*, 2004, **30–31**, 107–114.
- 47 F. Giordanino, E. Borfecchia, K. A. Lomachenko, A. Lazzarini, G. Agostini, E. Gallo, A. V. Soldatov, P. Beato, S. Bordiga and C. Lamberti, *J. Phys. Chem. Lett.*, 2014, **5**, 1552–1559.
- 48 L. Ma, Y. Cheng, G. Cavataio, R. W. McCabe, L. Fu and J. Li, *Appl. Catal., B*, 2014, **156–157**, 428–437.
- 49 T. Simons, P. Chen, D. Rauch, R. Moos and U. Simon, *Sens. Actuators, B*, 2016, **224**, 492–499.
- 50 S. Brandenberger, O. Kröcher, A. Wokaun, A. Tissler and R. Althoff, *J. Catal.*, 2009, **268**, 297–306.
- 51 J. Dědeček, L. Čapek, P. Sazama, Z. Sobalik and B. Wichterlová, *Appl. Catal., A*, 2011, **391**, 244–253.
- 52 F. Gao, D. Mei, Y. Wang, J. Szanyi and C. H. F. Peden, *J. Am. Chem. Soc.*, 2017, **139**, 4935–4942.
- 53 L. Chen, T. V. W. Janssens, P. N. R. Vennestrom, J. Jansson, M. Skoglundh and H. Grönbeck, *ACS Catal.*, 2020, **10**, 5646–5656.
- 54 T. V. W. Janssens, H. Falsig, L. F. Lundegaard, P. N. R. Vennestrom, S. B. Rasmussen, P. G. Moses, F. Giordanino, E. Borfecchia, K. A. Lomachenko, C. Lamberti, S. Bordiga, A. Godiksen, S. Mossin and P. Beato, *ACS Catal.*, 2015, **5**, 2832–2845.
- 55 K. A. Lomachenko, E. Borfecchia, C. Negri, G. Berlier, C. Lamberti, P. Beato, H. Falsig and S. Bordiga, *J. Am. Chem. Soc.*, 2016, **138**, 12025–12028.
- 56 L. Chen, H. Falsig, T. V. W. Janssens and H. Grönbeck, *J. Catal.*, 2018, **358**, 179–186.
- 57 E. Borfecchia, C. Negri, K. A. Lomachenko, C. Lamberti, T. V. W. Janssens and G. Berlier, *React. Chem. Eng.*, 2019, **4**, 1067–1080.
- 58 C. Paolucci, I. Khurana, A. A. Parekh, S. Li, A. J. Shih, H. Li, J. R. Di Iorio, J. D. Albarracin-caballero, A. Yezerets, J. T. Miller, W. N. Delgass, F. H. Ribeiro, W. F. Schneider and R. Gounder, *Science*, 2017, **903**, 898–903.





- 59 X. Wang, L. Chen, P. N. R. Vennestrom, T. V. W. Janssens, J. Jansson, H. Grönbeck and M. Skoglundh, *ChemCatChem*, DOI: [10.1002/cctc.202100253](https://doi.org/10.1002/cctc.202100253).
- 60 N. Zhu, Y. Shan, W. Shan, Y. Sun, K. Liu, Y. Zhang and H. He, *Environ. Sci. Technol.*, 2020, **54**, 15499–15506.
- 61 J. Han, A. Wang, G. Isapour, H. Härelind, M. Skoglundh, D. Creaser and L. Olsson, *Ind. Eng. Chem. Res.*, 2021, **60**, 17826–17839.
- 62 M. Koebel, G. Madia and M. Elsener, *Catal. Today*, 2002, **73**, 239–247.
- 63 J. M. Fedeyko, B. Chen and H. Y. Chen, *Catal. Today*, 2010, **151**, 231–236.
- 64 O. Mihai, C. R. Widyastuti, S. Andonova, K. Kamasamudram, J. Li, S. Y. Joshi, N. W. Currier, A. Yezerets and L. Olsson, *J. Catal.*, 2014, **311**, 170–181.
- 65 J. H. Lee, Y. J. Kim, T. Ryu, P. S. Kim, C. H. Kim and S. B. Hong, *Appl. Catal., B*, 2017, **200**, 428–438.
- 66 M. Devadas, O. Kröcher, M. Elsener, A. Wokaun, N. Söger, M. Pfeifer, Y. Demel and L. Musmann, *Appl. Catal., B*, 2006, **67**, 187–196.
- 67 <https://webbook.nist.gov/cgi/cbook.cgi?ID=C10024972&Units=SI&Type=IR-SPEC&Index=1#IR-SPEC>.
- 68 B. Liu, D. Yao, F. Wu, L. Wei, X. Li and X. Wang, *Ind. Eng. Chem. Res.*, 2019, **58**, 20516–20527.
- 69 R. Ramprasad, W. F. Schneider, K. C. Hass and J. B. Adams, *J. Phys. Chem. B*, 1997, **101**, 1940–1949.
- 70 C. Negri, T. Selli, E. Borfecchia, A. Martini, K. A. Lomachenko, T. V. W. Janssens, M. Cutini, S. Bordiga and G. Berlier, *J. Am. Chem. Soc.*, 2020, **142**, 15884–15896.

